

## Characterising pore networks and their interrelation with the fibre architecture in unidirectional composites

Gomasasca, S.; Peeters, D.M.J.; Atli-Veltin, B.; Slange, Tjitse ; Ratouit , G.; Dransfeld, Clemens

**DOI**

[10.1016/j.compositesa.2024.108669](https://doi.org/10.1016/j.compositesa.2024.108669)

**Publication date**

2025

**Document Version**

Final published version

**Published in**

Composites Part A: Applied Science and Manufacturing

**Citation (APA)**

Gomasasca, S., Peeters, D. M. J., Atli-Veltin, B., Slange, T., Ratouit , G., & Dransfeld, C. (2025). Characterising pore networks and their interrelation with the fibre architecture in unidirectional composites. *Composites Part A: Applied Science and Manufacturing*, 190, Article 108669. <https://doi.org/10.1016/j.compositesa.2024.108669>

**Important note**

To cite this publication, please use the final published version (if applicable). Please check the document version above.

**Copyright**

Other than for strictly personal use, it is not permitted to download, forward or distribute the text or part of it, without the consent of the author(s) and/or copyright holder(s), unless the work is under an open content license such as Creative Commons.

**Takedown policy**

Please contact us and provide details if you believe this document breaches copyrights. We will remove access to the work immediately and investigate your claim.



# Characterising pore networks and their interrelation with the fibre architecture in unidirectional composites

S. Gomasasca <sup>a</sup>,\* , D.M.J. Peeters <sup>a</sup>, B. Atli-Veltin <sup>a,b</sup>, T. Slange <sup>c</sup>, G. Ratouit <sup>c</sup>,  
C. Dransfeld <sup>a</sup>

<sup>a</sup> Department of Aerospace Structures and Materials, Delft University of Technology, Kluyverweg 1, 2629 HS Delft, Netherlands

<sup>b</sup> SRON Netherlands Institute for Space Research, Niels Bohrweg 4, 2333 CA Leiden, Netherlands

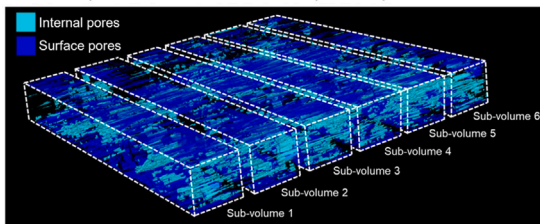
<sup>c</sup> Toray Advanced Composites, G. van der Muelenweg 2, 7443 RE Nijverdal, Netherlands

## GRAPHICAL ABSTRACT

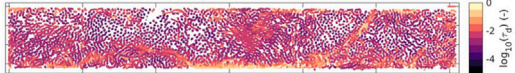
Characterising pore networks and their interrelation with the fibre architecture in unidirectional composites

TU Delft

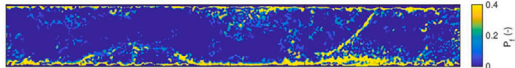
Analysis of X-ray micro-computed tomography data of thermoplastic/CF unidirectional composite tapes



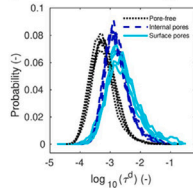
Fibre differential tortuosity



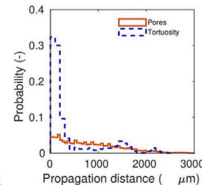
Pore fraction distribution



Higher probability of pores in tortuous regions



Lengthscale of feature propagation beyond sub-volume size



## ARTICLE INFO

### Keywords:

Carbon fibres  
Polymer-matrix composites (PMCs)  
Porosity/voids  
X-ray computed tomography

## ABSTRACT

This work proposes a methodology for the characterisation of complex pore features in unidirectional composite prepregs, and provides insights into the interaction between fibre architecture and pores. The method showcased allows to compare spatial distributions at a three-dimensional level, highlighting in the tape analysed a significant correspondence between regions of elevated tortuosity and increased pore fractions. Regions associated with highly tortuous meandering fibres exhibit a pronounced association with porosity located both in the bulk and at the tape surface, suggesting a strong interaction between non-collective fibre displacement and the probability of pore location. Furthermore, our study quantifies the length scale of feature propagation, shedding light on the spatial extent of microstructural pore occurrence within the composite.

\* Corresponding author.

E-mail address: [S.Gomasasca@tudelft.nl](mailto:S.Gomasasca@tudelft.nl) (S. Gomasasca).

<https://doi.org/10.1016/j.compositesa.2024.108669>

Received 12 September 2024; Received in revised form 22 November 2024; Accepted 15 December 2024

Available online 20 December 2024

1359-835X/© 2024 The Authors. Published by Elsevier Ltd. This is an open access article under the CC BY license (<http://creativecommons.org/licenses/by/4.0/>).

These findings have significant implications from a characterisation perspective to aid modelling approaches and manufacturing processes for high-performance composite prepregs tapes.

## 1. Introduction

Unidirectional thermoplastic composites are materials with complex microstructural features. Recent studies revealed that microstructural analysis can be used to establish the relationship between the manufacturing parameters and the microstructural features [1]. The first step in this direction is the development of methodologies that allow the identification of relevant features and evaluate their interrelations in various scales. With this goal in mind, the authors have previously introduced novel metrics to characterise fibre architectures in unidirectional thermoplastic composite prepregs, which address fibre tortuosity, collective fibre bundling effects and fibre network interconnectivity [2].

Porosity is strongly related to material processing, mechanical performance, and quality assessment of composites. Recent studies emphasise the importance of understanding the spatial characteristics of surface evolution and porosity in tapes, particularly with respect to defect analysis and the development of intimate contact [3]. Pore evolution is also relevant to the study of deconsolidation and consolidation phenomena during material processing [4,5]. Interestingly, pores, conventionally considered defects, can be deliberately designed within thermoplastic prepregs to create pathways for easier through-thickness or in-plane air removal, influencing material design and optimisation [6].

The spatial morphology of the reinforcement was found to affect permeation in thermoplastic composites through-thickness impregnation [7]. Additional studies propose qualitative observation of a possible link between pore locations and fibre tortuosity at a single fibre resolution in unidirectional composite tapes [8] and misalignment derived from structure tensor analysis in unidirectional consolidated laminates [9]. The pore distribution may therefore not be randomised, but rather linked to other microstructural features. The quantification of the link between pores occurrence and fibre architecture characteristics should be further investigated.

Microstructural information of unidirectional composites can be successfully obtained by X-ray Computed Tomography techniques, which can allow to obtain three-dimensional (3D) insights into the pore morphology and distribution in composite laminates [5,10,11]. While recent work leveraging Computed Tomography-based techniques was able to highlight the in-situ mechanical response of composites in relation to kink band formation under compression in the presence of defects [9], a clearer understanding of the different scales of organisational features is required.

The goal of this work is to understand the interrelation of different microstructural features at the fibre and pore levels in unidirectional composite prepregs, by developing an analysis methodology for 3D X-ray micro-computed tomography data at a single fibre resolution. A development-grade material with a thermoplastic matrix with complex manufacturing-induced pore morphologies was used. The investigation leads to the quantification of local microstructural phenomena linking tortuosity and the spatial propagation of porosity. This study aims to better understand the microstructural characteristics in unidirectional thermoplastic composites, with implications for manufacturing processes and material properties.

## 2. Methodology

This section describes the methodology followed for analysing 3D datasets of a unidirectional carbon fibre-reinforced composite prepreg. The data was obtained via X-ray microcomputed tomography and it was post-processed to extract information regarding the distribution of fibres and porosity.

### 2.1. Material

The unidirectional tape used is a development grade of Toray Cetex<sup>®</sup> TC1225 and was manufactured by Toray Advanced Composites. The tape used has standard modulus carbon fibre reinforcement and thermoplastic matrix. The material is the same used in previous work by Gomasca et al. [8]. A portion of the tape of about 2.5 mm in width measured orthogonal to the main fibre direction, and 10 mm along the main fibre direction was cut and used for microstructural analysis.

### 2.2. Tomographic image collection

The data was acquired via X-ray micro-computed tomography (XCT) with a Zeiss Xradia 520 Versa at Naturalis Biodiversity Center, Leiden. 3D volume acquisition was obtained with a 2000 × 2000 pixel detector in binning mode 1, 4x magnification lens, voltage of 70 kV, power of 5 W and an exposure time of 7 s. A schematic of the sample configuration during the measurement is provided in Fig. 1. The sample was mounted with the fibre principal alignment direction oriented vertically, and a detector-sample distance of 40 mm. The volume reconstruction was conducted with the software Scout-and-Scan™ Control System Reconstructor (Zeiss) as a standard reconstruction. The settings led to a voxel size of 0.7788 μm. The dataset is available at Ref. [12]. Three scan volumes have been stitched in the fibre length direction with an overlap of 21%, for a total scan volume length of about 3500 μm. Of that volume, a scan length of 3000 μm was selected for the analysis.

### 2.3. Segmentation of features of interest

The data was first reduced to 8 bits in Fiji [13] via linear scaling to reduce the computational cost, and then manually registered. This led to a volume used for the analysis measuring 1200 μm in the tape width (transversal to the fibre direction), 160 μm along the tape thickness and 3000 μm in the tape length (parallel to the main fibre direction).

To assess the spatial propagation of the features of interest, the total scan volume was split into six sub-volumes 500 μm long along the principal fibre alignment direction  $z$ . Representative cross-sections for Sub-Volume 1 are shown in Fig. 2. The tape orientation shown in Fig. 2, and the definition of a top and a bottom surface, do not relate to the tape orientation during manufacturing. The subdivision of the tape into individual sub-volumes allows the neglect of long-range variations in tape profile due to bending and rotation. The  $z$  direction was chosen as it is expected that unidirectional composites will present features that will be preferentially retained along that axis. All the analyses conducted, unless highlighted explicitly in the text, were performed based on the distinction between sub-volumes.

The objective of the segmentation step is to distinguish fibres and porosity. Fibre and pore space segmentation was performed in Fiji using the Weka Trainable Segmentation (Weka) plugin [14], which is a trainable machine learning tool that performs pixel-based segmentation. Segmentation was performed generating two distinct classifiers: one to identify fibres and one for recognising porosity and air surrounding the tape. A training set based on ten equidistant  $xy$  cross-sections extracted from the total scan volume of 3000 μm was used.

The obtained segmented images related to porosity were further processed via morphological operation of 3D opening with a 3D ball element of 1 voxel radius in Fiji to reduce noise in the segmentation.

Following the distinction between fibres, porosity and air surrounding the tape for each sub-volume, the following approach was implemented. First, close (internal) and open porosity regions are distinguished, and a global boundary for the tape at each sub-volume

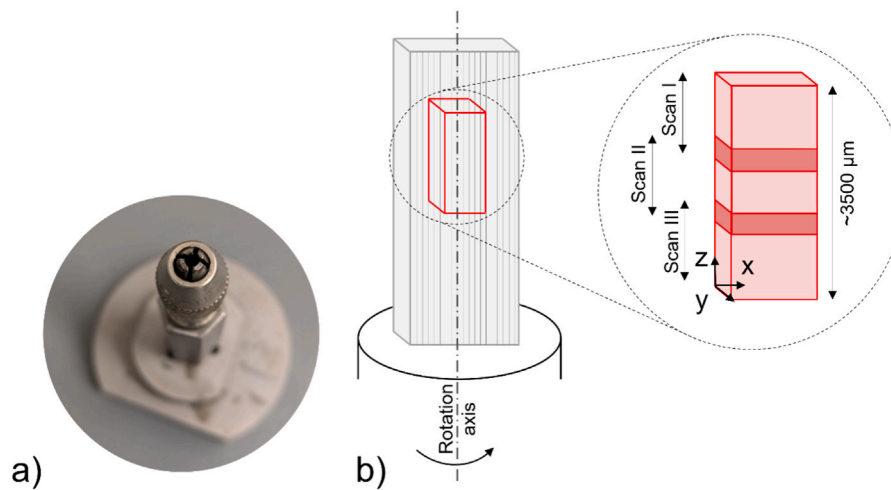


Fig. 1. (a) Detail of the sample holder used; (b) schematic of the sample mounting for the XCT measurement, and of the scanned region of interest. The z axis corresponds to the fibre principal alignment direction in the sample.

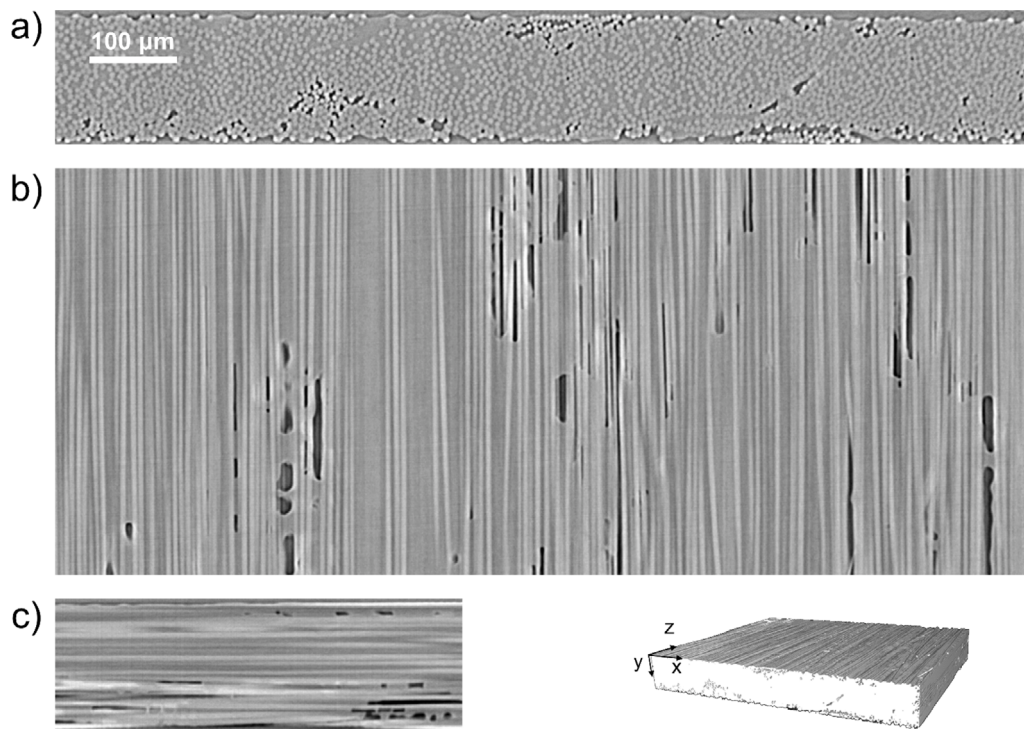


Fig. 2. Cross-sections derived from X-ray microcomputed tomography data for Sub-Volume 1, with reference to the planes (a)  $xy$ ; (b)  $xz$ ; (c)  $yz$ .

location was determined to identify open pore areas which pertain to the tape region, defined as surface pores. Secondly, the segmented fibres are converted into fibre path trajectories to further quantify the parameters of interest.

### 2.3.1. Internal and surface porosity

A 3D connected region analysis was conducted on the pore space in Matlab with the functions 'bwconncomp' and 'regionprops' to identify individual pores for further quantification. A 26-connectivity criterion was used for each voxel, which considers both faces, edges, and corners to touch in defining connected components.

Two categories of porosity can be distinguished. Internal (close) pores were defined as 3D regions entirely embedded in the tape. Complex open pore networks of non-impregnated areas are also observed, which communicate with the air surrounding the tape. The surface

porosity of pertinence to the tape was identified via the definition of a tape boundary for each sub-volume.

A schematic of the workflow conducted in Matlab for the tape boundary determination per sub-volume is shown in Fig. 3(a)-(c), in reference to the  $xy$  cross-sectional plane. The segmented tape profile for each  $xy$  cross-section within the individual sub-volume was first considered as in Fig. 3(a), where open pore regions are shown in black, and regions occupied by the tape are shown in white. To determine the tape boundary in each sub-volume, the fraction of voxels occupied by the tape for each location on the  $xy$  plane have been considered, as shown in Fig. 3(b). Voxels highlighted in yellow indicate certainty of belonging to a tape area throughout the entire sub-volume, while the ones shown in blue belong to open pore regions. A threshold of 0.07 was used to binarise the normalised count map, to exclude regions with a very low probability of locating inside the tape area,

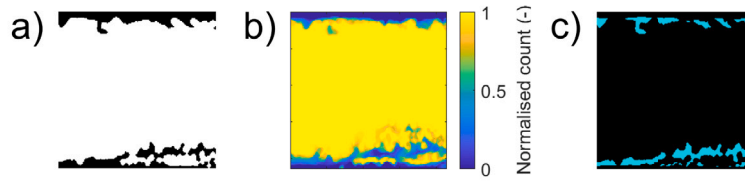


Fig. 3. Workflow for boundary extraction for Sub-volume 1: (a) segmented view where the regions showing open pores (black) and tape (white); (b) normalised count of voxels showing the likelihood a voxel to locate inside the tape area; (c) resulting surface porosity after boundary definition, shown in cyan.

and subsequently processed via a morphological operation of opening with a circular element of 3 voxels size as a noise removal step. The contour of the region identified was defined as boundary of the sub-volume and identified via the Matlab function 'bwtraceboundary'. The defined boundary represents the mesoscopic variability of the tape in each sub-volume. For each sub-volume, the connected pore regions falling between the boundary the  $xy$  cross-sections were defined as surface pores, which are shown in cyan in Fig. 3(c).

### 2.3.2. Fibre path reconstruction

Within the tape boundary for each sub-volume, the segmented cross-sections on the  $xy$  plane were averaged in groups of five (corresponding to a scan length of about  $39 \mu\text{m}$ ) as a data reduction scheme, as in previous work [2]. The resulting image stack was then analysed with Trackmate, a plugin available in Fiji that allows one to identify and track circular objects moving in 3D space, or time [15]. A detector employing a Laplacian of Gaussian filter and a reference fibre diameter of  $6 \mu\text{m}$  was applied to identify the fibre centres. The selected tracker for fibre reconstruction was based on the Simple Linear Assignment Problem [15], with a maximum linking distance between fibre centres of  $5 \mu\text{m}$ , an in-plane maximum gap-closing distance of  $5 \mu\text{m}$  and a gap-closing distance along the main fibre alignment direction of 45 data-reduced  $xy$  cross-sections (corresponding to an axial length of  $225 \mu\text{m}$ ). The gap-closing distance chosen is meant to facilitate fibre trajectory reconstruction in the presence of segmentation artefacts that might otherwise result in a partial portion of fibres not being recognised as one single entity. Detected fibres longer than  $60 \mu\text{m}$  were further analysed. While the fibres studied are in principle long and continuous, the threshold allows to include in the analysis partially captured fibres at the left and right sides of the tape moving in and out of the scan volume, fibres that might have a broken end, as well as portions of long fibres misinterpreted as separate fibre segments.

The fibre trajectories so obtained were further processed in Matlab. Non-defined values in the fibre trajectories have been reconstructed via the linear interpolation function 'fillmissing'. The fibre paths were then smoothed via local regression using weighted linear least squares and a 2nd degree polynomial model with an interpolation length of  $39 \mu\text{m}$ .

## 3. Quantification of metrics for the material description

### 3.1. Description of pore features

For each sub-volume, the variability in the distribution of porosity was first assessed by the local pore fraction  $P_f$ , determined on a voxel basis for the three projection planes  $xy$ ,  $zy$  and  $xz$  as the fraction of voxels occupied by pores at each cross-sectional location.

The geometrical characteristics of individual internal and surface pores were then quantified via ellipsoid approximation based on their principal semi-axes. The metrics proposed in the work of Mehdikhani et al. [10] were used for comparison, namely Roundness (R), Geometrical Mean (GM) and Elongation (E):

$$R = \frac{c}{b} \quad (1)$$

$$GM = (cb)^{1/2} \quad (2)$$

$$E = \frac{a}{GM} \quad (3)$$

where  $a$ ,  $b$ , and  $c$  are the semi-major, semi-medior and semi-minor axes of the approximated ellipsoid. Pores with a volume greater than 1 voxel were considered for this analysis.

### 3.2. Fibre differential tortuosity

The differential tortuosity of fibres was defined as in previous work [2,8]:

$$\tau^d = \frac{L}{L_0} - 1 \quad (4)$$

where  $L$  is the fibre length, and  $L_0$  is the length of the scan space in the principal fibre alignment direction over which  $L$  is evaluated. The parameter represents the trajectory deviation of a fibre from a perfectly straight path in the principal alignment direction. A fibre perfectly aligned to the main fibre direction will have a tortuosity of zero. The more alignment is lost in the fibre, or the more the angular deviation from the alignment direction is, the more tortuosity will increase. The logarithm of tortuosity will be considered in the analysis.

In this work, differential tortuosity was calculated on a sliding window aligned with the principal fibre alignment direction  $z$  of  $L_0 = 43 \mu\text{m}$ , equivalent to approximately 6–7 times the fibre diameter. The value was considered small enough to retain local properties, while allowing for an extent of local homogenisation and noise removal. A schematic of the calculation is shown in Fig. 4. The window of calculation moves along each fibre trajectory to account for varying fibre length and to obtain a 3D distribution of the parameter.

### 3.3. Data reduction of pore regions and differential tortuosity for feature correlation

In the sample studied, pores tend to locate in-between fibres as qualitatively visible in Fig. 2. Local tortuous behaviour might influence pore locations, and possibly create far-field effects. To study possible correlation of tortuosity and pore locations, the following method was developed. A max-filter was applied both on the binarised segmented pore volume and on the linearly interpolated differential tortuosity values as an image processing step to consider a translation tolerance for the compared features. Subsequently, differential tortuosity was compared at a voxel level to pore-free, internal, and surface porosity regions.

An example of image processing induced by the max-filter operation is shown in Fig. 5 for the case of the porosity distribution. The max-filter works through a moving kernel, over which only the maximum value is retained. In this work, a cubic kernel of 15 voxels on each side (equivalent to  $11.7 \mu\text{m}$ , about 1.5 times the fibre diameter) was used as a moving window across the volume, with a stride of 15 voxels and no padding. A sensitivity analysis on the effect of the kernel size can be found in the Supplementary Material.

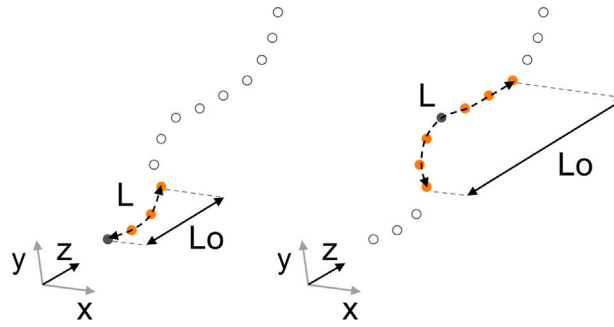


Fig. 4. Schematic for the calculation of differential tortuosity: represented on the left is the edge of the fibre, on the right at the centre of the fibre. In black is shown the point of calculation of local tortuosity, and in orange the window of calculation over the distance  $L_o$  aligned to the principal alignment direction  $z$ .  $L$  is the length measured along the fibre trajectory.



Fig. 5. (a) Segmented porosity cross-section on the  $xy$  plane, where pores are highlighted in white; (b) same cross-section after max-filtering with a cubic element of 15 voxels side, corresponding to approximately 1.5 times the fibre diameter.

### 3.4. Determination of characteristic lengthscales of differential tortuosity and pore regions

The propagation of porosity and differential tortuosity along the volume studied was assessed via the determination of their characteristic lengthscales based on spatial similarities of  $xy$  cross-sections of the max-filtered parameters. The use of spatial similarity analysis was used in the study of tow-based discontinuous composites via cross-correlation equations to extract information on the characteristic lengthscale of strain fields [16] and in unidirectional composites to study fibre misalignment in microscopy images [17]. Alternative ways for detecting similarity in arrays are Sum of Square Differences [18], Sum of Absolute Differences [19], and Euclidean Distance [20], which are conceptually similar approaches that can be applied to observe parameter variations at a voxel level. In this work, feature similarity analysis was conducted on binarised volumes by considering a normalised Sum of Absolute Differences (nSD) formulation:

$$nSD(z_i, z_j) = \frac{1}{N_{ij}} \sum_{k=1}^{N_{ij}} |(A_i)_k - (A_j)_k| \quad (5)$$

where  $z$  is the principal fibre alignment direction,  $A_i$  and  $A_j$  are two binarised cross-sections at locations  $i$  and  $j$  along  $z$  and  $N_{ij}$  is the combined number of voxel locations related to the feature observed for the two cross-sections (for the pore network, the pore voxel locations; for the tortuosity distribution, the voxels with value greater than the median). In the case of a binarised volume, the range of nSD goes from 0, indicating no change in the voxel values between the two slices, to 1, indicating a change in all voxels considered. A schematic of the calculation applied on a simplified case study is reported in Fig. 6.

## 4. Results and discussion

### 4.1. Porosity

#### 4.1.1. Quantification of cross-sectional pore clustering

Fig. 7(a1), (a2) and (a3) show the porosity fraction  $P_f$  determined for each voxel location on the projection planes  $xy$ ,  $xz$  and  $yz$  for Sub-volume 1. The maps corresponding to all sub-volumes can be found in the Supplementary Material (Section 1).

The pore fraction maps highlight that pores are not distributed homogeneously in the three projection planes considered for each sub-volume. On the  $xy$  plane high pore fraction regions tend to appear at discrete cross-sectional locations. The  $yz$  plane shows an edge-core effect in the distribution of the porosity fraction, with a higher pore fraction on the top and bottom surfaces of the tape. On the  $xz$  plane, the porosity fraction appears more homogeneously distributed.

Based on the pore fraction distributions on the three reference planes  $xy$ ,  $yz$  and  $xz$ , the extent of pore clustering on each of the three planes have been evaluated. Pore clustering indicates the extent to which pores are located in a limited (clustered) region on a reference plane or whether they are more homogeneously distributed. To quantify this characteristic, the fraction of the reference plane occupied by regions with  $P_f \geq 0.4$  (meaning that pores occupy more than 40% of the voxels at those cross-sectional locations), and by low pore fraction regions with  $P_f \leq 0.01$  (corresponding to less than 1% pores), were evaluated. The results are shown respectively in Fig. 7(b1) and (b2). The  $xy$  plane shows both the highest percentage of high- $P_f$  regions, up to 7% compared to less than 1% for the  $yz$  and  $xz$  planes, and the highest percentage to low- $P_f$  regions, up to 80% compared to less than 20% for the  $yz$  and  $xz$  planes. Clustering of high  $P_f$  regions on the  $xy$  plane, compared to  $yz$  and  $xz$ , suggests a preferential global orientation of the pore network with the main fibre direction  $z$  and a greater spatial variability of the porosity distribution across the tape width. The results were consistent for all sub-volumes, supporting the choice of  $z$  as the direction of feature propagation in Section 3.4.

#### 4.1.2. Geometrical analysis of internal and surface pores

A 3D view highlighting the different cross-sectional distributions of internal and surface pores for Sub-volume 1 is shown in Fig. 8(a). The through-thickness edge-core distribution of the pore fraction shown in the previous section in Fig. 7(a3) was observed in more detail in Fig. 8(b), where each line for each pore class refers to a different sub-volume. Consistently for each sub-volume, a higher pore fraction was found on the bottom side of the tape, and it can be mainly attributed to surface pores. Internal porosity appears less pronounced but shares the tendency to an edge-core effect, which overlaps with the through-thickness locations of surface pores. Fig. 8(c) highlights that

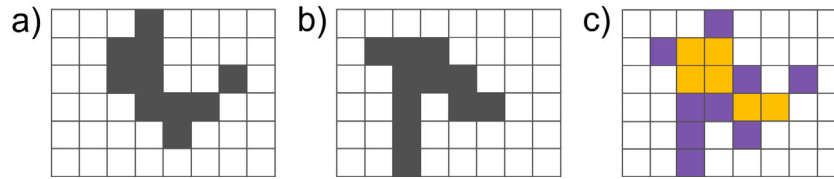


**Fig. 6.** Simplified example of the application of the similarity method (a) slice  $A_i$ , pore voxels highlighted in grey; (b) slice  $A_j$ , pore voxels highlighted in grey; (c) resulting map of nSD values for the global pore voxels in the two slices, counting a global number of pore locations  $N_{ij} = 15$ . The intersection of the pore regions are highlighted in orange (6 voxels), while the regions not overlapping are shown in purple (9 voxels), resulting in a value of  $nSD = 9/15 = 0.6$ .

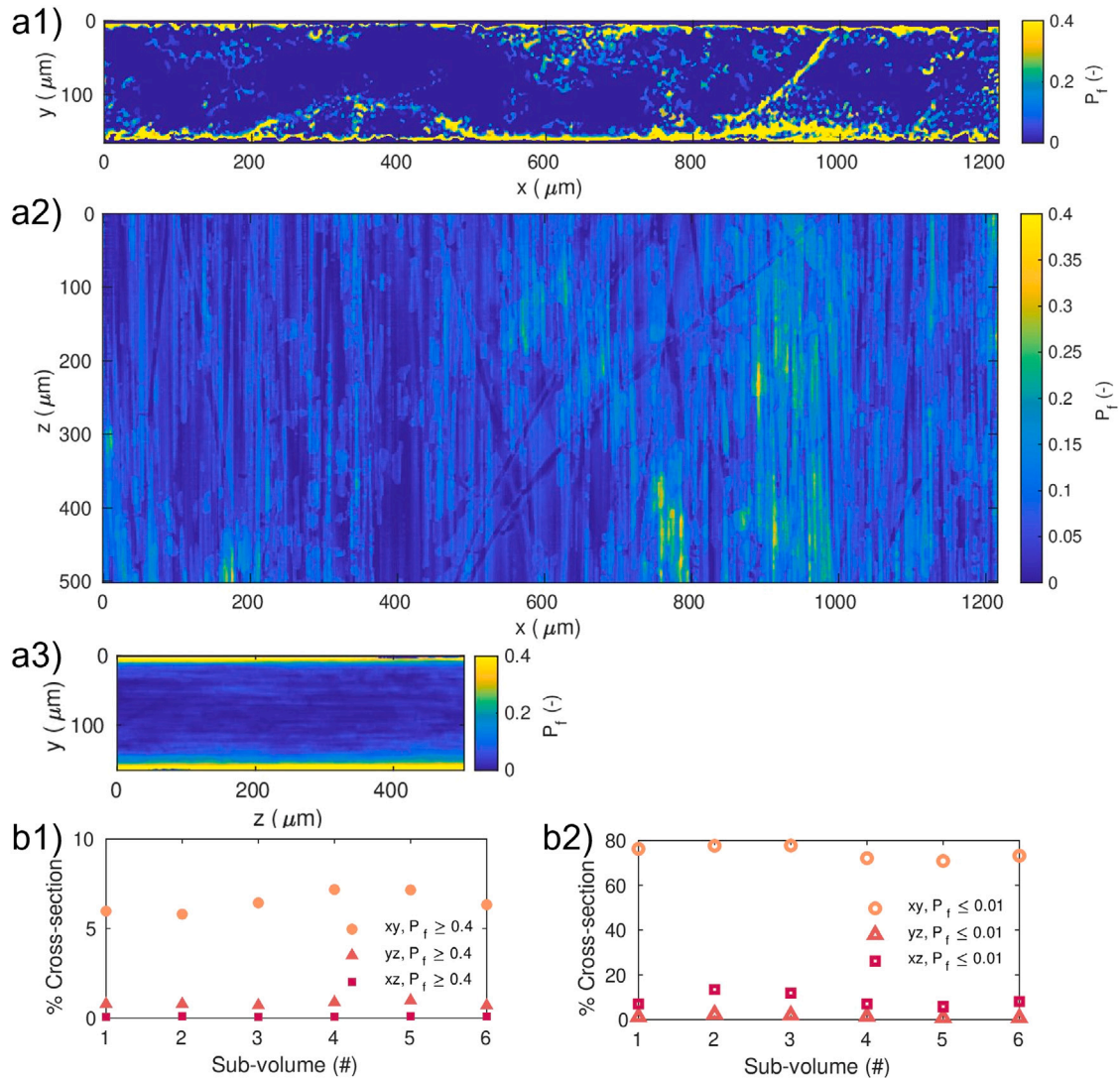


**Fig. 7.** For Sub-volume 1, pore fraction ( $P_f$ ) maps for the three projection planes (a1)  $xy$ , (a2)  $xz$  and a3)  $yz$ ; for all sub-volumes and the three projection planes, fraction of cross-section occupied by (b1) high pore fraction ( $P_f \geq 0.4$ ) and (b2) low pore fraction ( $P_f \leq 0.01$ ).

the thickness affected by surface porosity can exceed half the thickness of the tape. However, no connected pore paths were found between the top and the bottom surfaces.

The morphology of internal and surface pores was analysed based on ellipsoid approximation in Fig. 9, which shows the aggregated results from the entire scan volume, in this case without considering the artificial boundaries created by the subdivision in distinct sub-volumes. The three parameters considered are compared to the pore volume  $V_p$ , shown on the horizontal axis, which is measured based on pore voxels, and each pore is shown as a single datapoint. Roundness decreases from a value of 1 (perfectly circular cross-section) towards a value of

zero (flattened cross-section) with increasing pore volume  $V_p$  for both internal and surface pores, as seen in Fig. 9(a). Surface pores tend to be flatter at the same volume than internal pores. The Geometrical Mean of the two smaller semi-axis shown in Fig. 9(b), which indicates the size of the pore cross-section, increases with  $V_p$ . A similar parameter trend is found for internal and external pores in log-log scale, but with a larger range for surface pores. Elongation, which relates the major semi-axis to the Geometrical Mean, also increases with  $V_p$ , at a higher rate for surface pores than for internal pores, as shown in Fig. 9(c). The result indicates the general tendency of larger pores to have a higher aspect ratio between their length and cross-sectional dimension. Additional

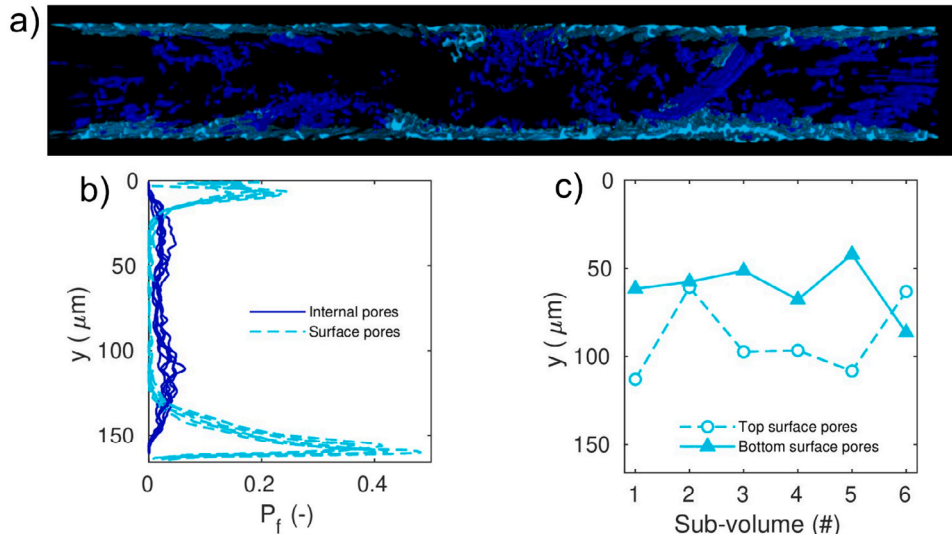


Fig. 8. Distinction between internal and surface pores (a) 3D representation for Sub-volume 1 of internal pores (in cyan) and surface pores (blue); (b) through-thickness pore fraction  $P_f$ ; (c) coordinate of the maximum inner edge of the top and bottom surface pores.

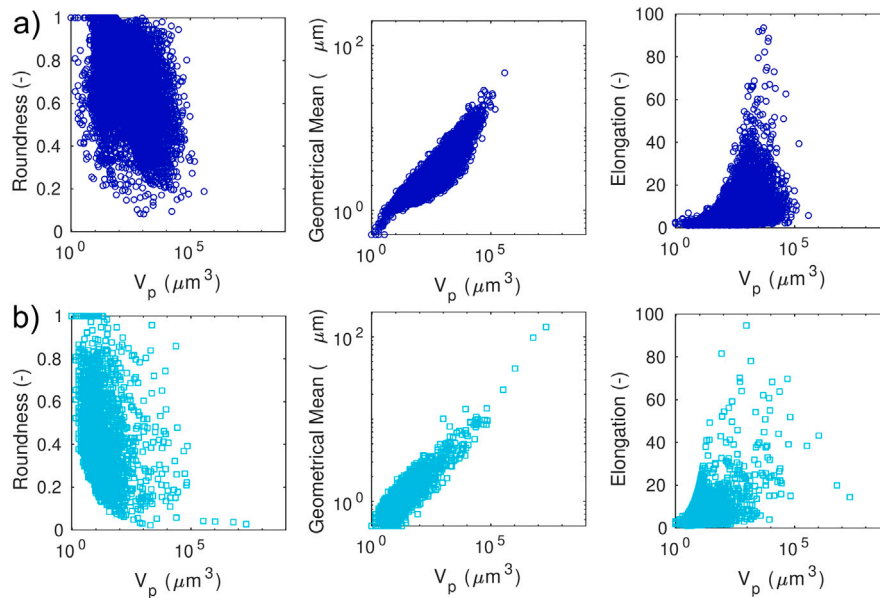


Fig. 9. Geometrical characteristic of pores as a function of pore volume ( $V_p$ ) for the full scan, for (a) internal pores; (b) surface pores. Pore volume and Geometrical mean are expressed in logarithmic scale.

information on the statistics of internal and surface pores can be found in the Supplementary Material (Section 2).

#### 4.1.3. Implications on tape manufacturing processes

The methodology here developed for the porosity description in freestanding unidirectional composite tapes allowed to highlight features of relevance for tape manufacturing control. The tape boundary definition used to identify surface porosity enabled the identification of both surface pores affecting the inner tape portions and surface pores more strongly related to the surface topology of the tape. The boundary definition for each sub-volume highlighted an overall straight geometry of the top and bottom tape surfaces, as visible in Figs. 3(c) and 8(a). Surface pores at the top and bottom edges and internal pores constitute a discontinuous network. The tape manufacturing process and consolidation step strongly influence surface porosity. Similar complex surface pore features have been reported in the manufacturing of thermoplastic prepregs from aqueous polymer slurry [6], and the

methodology proposed in this work show the potential to further explore the characteristics of such materials in relationship to their performance.

Pores developing through the tape thickness are expected to negatively affect the local transverse strength of the tape; however, in the case of surface pores, they might provide advantages for air evacuation during subsequent processing, as seen in the case of partially impregnated prepregs [6]. The surface porosity related to the topological variability of the tape is instead more strongly associated with the roughness of the tape surface. In the case studied, where the tape surface is matrix-poor, local fibre path deviations from the main alignment direction  $z$  of the exposed fibres on the tape surface can be qualitatively observed, which is expected to influence both the tape surface roughness, and the consolidation performance [21]. The portion of surface pores linked to roughness is expected to disappear during part manufacturing and might positively contribute towards intimate contact development [3].

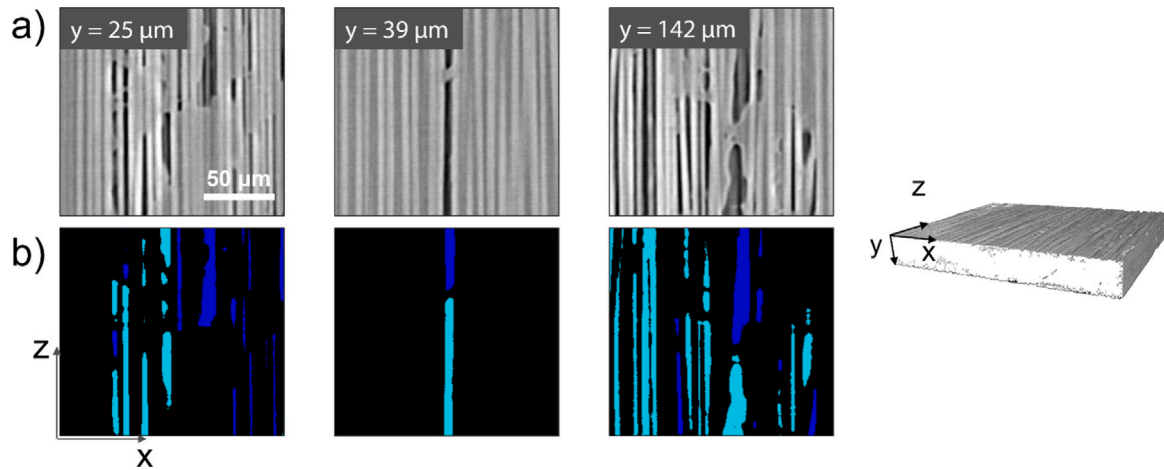


Fig. 10. Examples from Sub-volume 1 of (a)  $xz$  cross-sections of the scan volume; (b) corresponding segmented pore views, indicating internal pores in dark blue and surface pores in cyan. The full cross-sections are available in the Supplementary Material (Section 3).

Details of the spatial arrangement of pores on the  $xz$  plane are represented in Fig. 10, and more extensive examples are provided in the Supplementary Material (Section 3). Both internal pores (in blue) and surface pores (in cyan) might appear on  $xz$  cross-sections as separate ‘collapsed’ entities aligned in the principal fibre direction  $z$  inbetween the same fibres. Similar pore formations were observed in unidirectional thermoset composites as a result of the collapse of larger pores [22]. It is therefore possible that in the tape here analysed the same features might similarly originate from the degeneration of larger pores during processing. In particular, Fig. 10 highlights that surface and internal pores are found at multiple locations to align along the  $z$  direction in close proximity, which suggests that part of the internal pore population could originate from the collapsed surface porosity. Overlaps between internal and surface pores were shown in their through-thickness distribution in Fig. 8(b) and in the cross-sectional clustering on the  $xy$  plane in Fig. 7(a), further suggesting that propagation between the two pore classes. The portion of surface pores entering the tape thickness might be more closely related to pore network propagation to internal porosity, and might favour air evacuation during consolidation [6]. The hypothesis formulated through the tape analysed could be applied to further understand the tape manufacturing process in the mechanisms of porosity evolution during resin impregnation.

#### 4.2. Differential tortuosity

Differential tortuosity  $\tau_d$  was evaluated for each fibre at a local level to obtain a 3D distribution of the parameter. Fig. 11(a) shows a projection on the  $xy$  plane of the maximum differential tortuosity values for each fibre in Sub-Volume 1, highlighting the cross-sectional variability of the parameter in logarithmic scale. Values of  $\log_{10}(\tau_d) \geq 0$  shown in yellow indicate highest tortuosity values of 1, while  $\log_{10}(\tau_d) \geq -4$  in purple indicate values of tortuosity of 0.0001. The tortuosity maps corresponding to all sub-volumes can be found in the Supplementary Material (Section 4).

Some fibres are observed to move along trajectories with high tortuosity and misalignment, traversing the tape thickness or migrating along the bottom surface. Two such high-tortuosity fibres traversing the region marked with a black dashed square in Fig. 11(a) are highlighted in Fig. 11(b) in magenta and blue respectively, at two different locations along the tape length  $z$ . The trajectories of both fibres appear to intercept pore locations, visible in a darker colour in the greyscale image.

The through-thickness distribution of local tortuosity shown in Fig. 11(c) highlights an edge-core effect with higher tortuosity at the tape surfaces, especially pronounced in the 97.5% quantile of the distribution, consistently for all sub-volumes.

#### 4.3. Relationship between pore distribution and fibre tortuosity

Qualitative observations of a correspondence of the spatial distribution of both pores and tortuosity for Sub-Volume 1, corresponding to a lengthscale of 500  $\mu\text{m}$ , can be seen in the projection plane  $xy$  by comparing Fig. 7(a) with Fig. 11(a) and (b). Higher tortuosity can be found at similar cross-sectional locations of higher pore fraction regions. The same observations can be extended for all sub-volumes with reference to the Supplementary Material (Sections 1 and 4), suggesting that possible correspondences between tortuosity and pore distribution might remain valid both at a local and over longer length-scales, possibly due to the propagation of both parameters along the main fibre alignment direction.

Further indication of a correspondence of the two descriptors can be provided by their through-thickness edge-core effect, with higher porosity and tortuosity at the tape edges, shown in Figs. 8(b) and 11(e). On the very tape surfaces, the greater freedom of fibre displacement translates to higher tortuosity, causing surface topological changes which are included in the definition of surface pores here proposed. In the case of thermoset unidirectional composite processing, pores can get trapped between fibres closer than a characteristic threshold [23], which is the case where high tortuosity and misalignment are present in conjunction to high fibre volume content. Comparable effects could be induced during thermoplastic tape manufacturing in the presence of similar features of the fibre architecture, depending on the impregnation strategy.

##### 4.3.1. Correlation of pore distribution and fibre differential tortuosity

The 3D distributions of tortuosity, internal pores and surface pores were data-reduced by max-filtering as described in Section 3.3, and compared on a voxel-by-voxel basis. For each pore voxel, and for each pore-free voxel, the corresponding value of tortuosity was reported in Fig. 12(a) with differential tortuosity shown in logarithmic scale. Each line shown represents a distinct sub-volume. In the material studied, the methodology proposed was able to capture that distribution of tortuosity values intercepted by internal and surface pores shows a shift towards higher values compared to pore-free regions, consistently for all sub-volumes. In particular, regions with the highest range of tortuosity  $\log_{10}(\tau_d) \geq -2$  (corresponding to  $\tau_d \geq 0.01$ ) are found in surface pores and internal pores, but not in pore-free regions, highlighting the relevance of high tortuosity features on the pore population. In particular, surface pores are shown to have a larger tail of the distribution towards higher tortuosity values, suggesting a greater influence compared to internal pores. The results show consistency across the six sub-volumes, indicating that the conclusion is valid over an extended

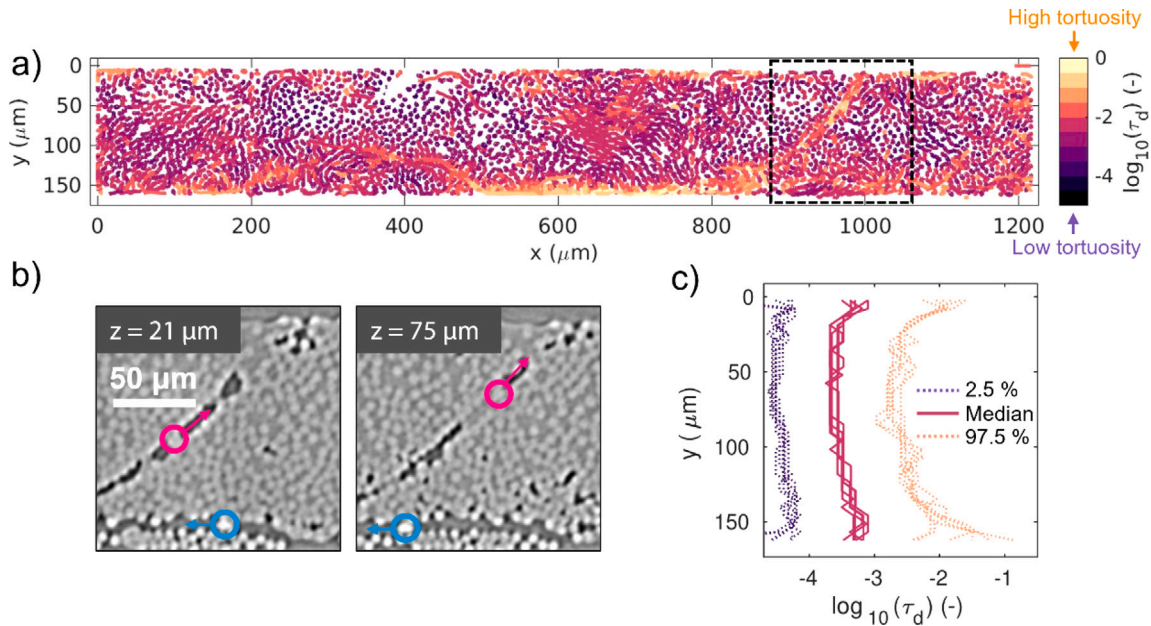


**Fig. 11.** (a) Cross-sectional distribution of the logarithm of differential tortuosity for Sub-volume 1, where each fibre path is projected on the  $xy$  plane and colour-coded depending on their maximum local tortuosity value; (b) two fibre centres with visible ovalization in high-tortuosity, one highlighted in magenta and one in blue, tracked at two  $z$  locations in the blue dashed regions in (a); (c) through-thickness distribution of differential tortuosity, each line corresponding to a different sub-volume. The median value, 2.5% quantile and 97.5% quantile are highlighted for each sub-volume.

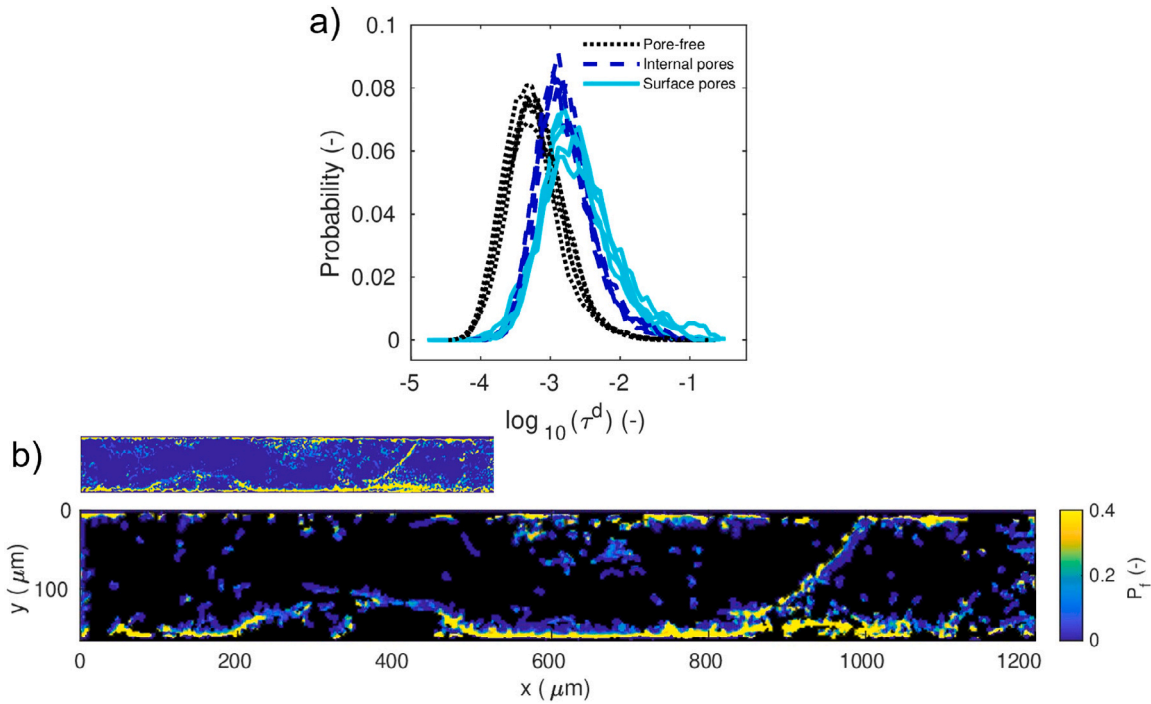


**Fig. 12.** (a) Differential tortuosity values in correspondence of pore-free regions, internal pores and surface pores for all sub-volumes; (b) above: miniature image recalling the pore fraction distribution on the  $xy$  plane for Sub-volume 1 shown in Fig. 7 (a1); below: the same pore fraction distribution was masked in black, to display in colour only the pore probability overlapping to fibre trajectories in the higher tortuosity range with a maximum  $\log_{10}(\tau_d) \geq -2$ .

lengthscale.

An added advantage of using data reduction is that small shifts between parameters are automatically taken into account. In principle, no fibres (hence, not tortuosity values) are present at exact pore locations, preventing an effective correlation. Through max-filtering with an adequately sized kernel, the local microstructural information can be more easily compared. Max-filtering might restrict the range of tortuosity values by cutting its lower range, but it is expected to

locally enhance the visibility of areas of high tortuosity values to assess their influence on the surrounding microstructure, which is of value for the analysis. To clarify the effect of the max-filter element size results obtained, a sensitivity analysis was conducted as reported in Supplementary Material (Section 7). The results of the sensitivity analysis highlight that the results shown are still valid in the range of element sizes employed.

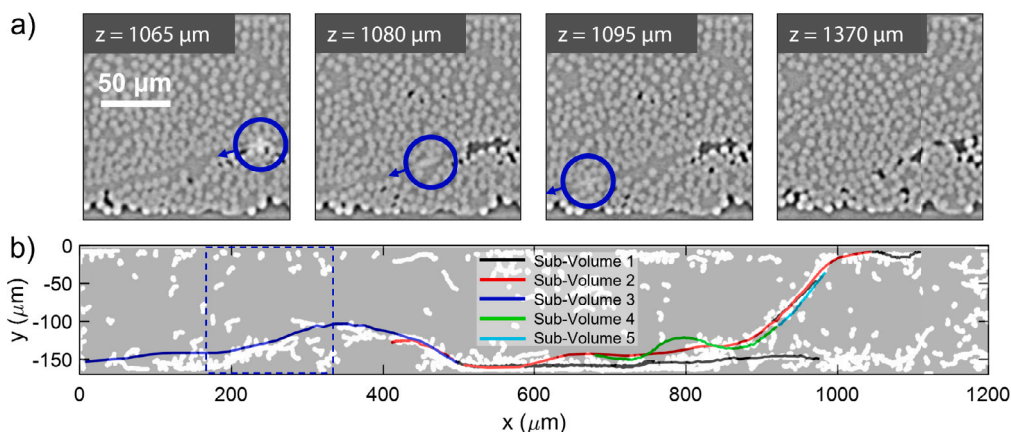


**Fig. 13.** (a) Meandering fibre visible inside the blue circle, at different locations along the tape length, and subsequent disappearance of the corridor generated in the last frame; (b) manually tracked meandering fibre paths for Sub-Volume 1 to 5 projected on the  $xy$  plane, overlapping to the fibre trajectories with a maximum  $\log_{10}(\tau_d) \geq -2$  for Sub-Volume 1, shown in white. The cross-sectional region shown in (a) is highlighted in a dashed square.

A possible explanation of a relationship between tortuosity and pore distribution is at the level of microstructure formation, as anticipated in Section 4.1.2. Regions with higher local tortuosity could generate cavities and barriers to resin flow during impregnation [23], creating far-field effects on the pore evolution. Furthermore, pore pressure can impose significant fibre movement in the case of thermoset matrices [23], and a similar effect might occur in higher viscosity systems such as thermoplastic matrices. Pore evolution might therefore also influence to a degree the local fibre architecture in its immediate surroundings. Features such as collective bundling effects of fibres, fibre network connectivity [2], fibre neighbours contacts [2,24,25] and local fibre volume fraction could also impact the pore distribution and should be addressed in future research to improve our understanding of the mechanisms of microstructure formation.

#### 4.3.2. Meandering fibres in high-tortuosity regions

The methodology developed highlighted strong interactions between high-tortuosity regions and the pore distribution. For the tape studied, the fibres in the highest tortuosity range move along preferential corridors running transversally to the thickness of the tape and along its lower edge with high misalignment from the principal fibre alignment direction. Examples are provided in Figs. 11(b) and 13(a). Since pores appear linked to high tortuosity regions in the tape studied, meandering fibres populating high tortuosity corridors constitute a key feature.

Such meandering fibres represent mechanically weaker points in the tape, and might initiate fracture [26], but might also lead to crack branching [27]. Furthermore, because carbon fibres are conductive, through-thickness fibre migration could constitute topology-dependent electrical percolation pathways [28] with possible consequences on the electrical conductivity of prepregs for processing techniques such as induction welding. Meandering fibres constitute, therefore, a disruption of the microstructure that should be carefully controlled and tailored during manufacturing.

One possible hypothesis is that the presence of individual meandering fibres across the tape thickness might originate from local variations in tension across the fibre tow. Tension differences within the tow can occur during manufacturing; however, in the case of single meandering fibres, the loss of tension might result from the rupture of individual filaments on the tow surface due to frictional forces during dry tow spreading [29]. Limiting the degree of fibre breakage through control of the spreading process could, therefore, result in lower meandering fibres and more aligned microstructures, with reduced porosity events downstream in the manufacturing process.

Characterisation routes such as laser measurement units can be integrated as in-line techniques to aid in identifying broken fibres and

improving the manufacturing control [30]. Meandering fibres traversing the thickness of prepregs with conductive fibre reinforcement, such as carbon fibres, could be identified via electrical conductivity measurements based on six-probe methods [28] and Eddy current testing [31]. In the application of 3D techniques such as lower resolution X-ray micro-computed tomography analysed with structure tensor method [32] and X-ray scattering tensor tomography [33], care should be used in avoiding excessive homogenisation of the microstructural information, as single fibre triggering events for larger scale phenomena might otherwise get missed.

Meandering fibres show high cross-sectional ovalization on the  $xy$  plane and appear to move along resin-rich corridors, as also reported in the work of Yu et al. for highly misaligned fibres [34]. Local ordering effects are observed around such corridors, consisting of fibre alignment along the sides of the trajectory of meandering fibres, which are retained both before and after its passage. The meandering fibre highlighted in Fig. 13(a), which corresponds to the blue curve in 13(b) in Sub-Volume 3, appears in the field of view shown at about  $z = 1065 \mu\text{m}$  and exits it at  $z = 1095 \mu\text{m}$ , however, the corridor effect generated along its passage can be qualitatively observed to disappear only  $270 \mu\text{m}$  further in the principal alignment direction, at about  $z = 1370 \mu\text{m}$ . In general, the lengthscale affected by the transit of a meandering fibre is observed to be influenced by the tortuosity of the fibre. The local ordering effect around resin corridors left by fibres with high tortuosity and misalignment might be related to far-field effects on the surrounding microstructure and cause greater disruption in regions with high fibre volume fraction, which is the case in this work.

In the workflow used, the detection of meandering fibres is a tedious process due to their out-of-average behaviour. Trackmate might not recognise high tortuosity fibre correctly especially in the case of high ovalization of their transversal cross-section. A careful selection of the “gap closing distance” was useful to link partially detected portions of a fibre, however, loss of information was still observed. The trajectories of some manually-tracked meandering fibres located in a high-tortuosity corridors in five consecutive sub-volumes are here reported Fig. 13(b). The trajectories of some of those fibres span multiple volumes. A view of the manually traced fibres on the  $xz$  projection plane is shown in the Supplementary Material (Section 5). The fibres shown were only partially detected in the automated fibre extraction step. The microstructural information shown in Fig. 11(a), compared to the manually tracked fibres in Fig. 13(b), suggests that the overall effect of the high-tortuosity corridors was still conveyed in the analysis at the sub-volume scale. If more accuracy was needed in future work to strengthen the analysis further, the authors recommend image-pre processing techniques to facilitate distinguishing misaligned

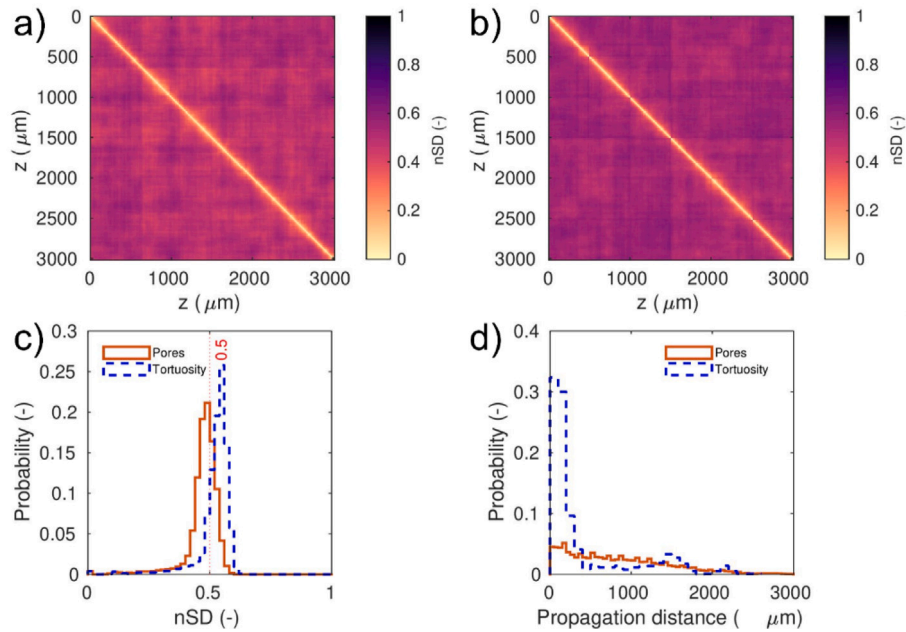


**Fig. 14.** Distance map of the similarity score nSD for the full scan volume in relation to the  $xy$  plane and a cubic max-filtering element of 15 voxel side for (a) pores and (b) differential tortuosity; (c) histogram of the similarity score nSD for pore network and high differential tortuosity, with the selected threshold of evaluation at  $nSD = 0.5$  highlighted in a red dashed line; (d) lengthscale of feature propagation for pore and tortuosity regions falling in the range  $0 \leq nSD \leq 0.5$ .

individual fibre trajectories at a 3D level [25,35], and finer post-processing strategies to link partial fibre segments, as shown elsewhere in the literature [36].

#### 4.4. Determination of the lengthscale of propagation for pore network and tortuosity

The methodology showcased in Section 4.3.1 highlighted a preferential location of pores in higher tortuosity regions, compared to pore-free areas, in the material used as the case study. In this section, a methodology to investigate the spatial evolution of the two features is applied to assess possible correspondences in their lengthscale of propagation, based on the method introduced in Section 3.4.

Fig. 14(a) and (b) show the distance map obtained by determining nSD with a cubic kernel of 15 voxel side for each pair of max-filtered slices across the full volume for differential tortuosity and pores, respectively. The distance map of the similarity score is symmetrical with respect to the top-left-bottom-right diagonal. The values of nSD along said diagonal are obtained by comparing a cross-section with itself, resulting in a perfect match and, hence, a value of nSD equal to 0, indicating no change in the parameter distribution. For the same case of a cubic max-pooling element of 15 voxel size, a summary of the similarity values for Fig. 14(a) and (b) is provided in the histograms of Fig. 14(c), which shows nSD in the range of 0 to 0.65 for both parameters. Based on the analysis performed in the Supplementary Material (Section 6), a value of  $nSD = 0.5$  was selected as a lower bound to assess feature similarity. At that value of nSD, half of the feature distribution is retained, while half has migrated to different locations. In this case, the 68% of the pore regions and the 19% of the high tortuosity regions fall in the range of nSD between 0 and 0.5, corresponding to the highest similarity range. The results indicate that while most pore regions propagate through the volume, at the scale observed high tortuosity regions show a greater local fluctuation.

The distribution of distances between  $xy$  cross-sections in which high similarity is encountered, hence with  $0 \leq nSD \leq 0.5$ , are reported in Fig. 14(d). For both the porosity network and high tortuosity regions,

propagation distances are found up to the range of 2000–3000  $\mu\text{m}$ , going beyond the limit of single sub-volumes and reaching the edge of the scan volume analysed. Data related to propagation distances beyond 2000  $\mu\text{m}$  should however be considered with caution due to the limit in the size of the scan volume and consequent low sampling in the range 2000–3000  $\mu\text{m}$ .

The distribution of propagation distances for the pore network is wider compared to the high tortuosity, suggesting a greater retention of characteristic features along the fibre length direction. The results of pore network similarity might be influenced by the criteria used to define surface porosity, which is based on a fixed tape boundary valid at each  $xy$  cross-section for a sub-volume and might, therefore, increase similarity within the sub-volume. However, since the distribution of propagation distances found is much longer than the 500  $\mu\text{m}$  length of each sub-volume and that it was taken into account in the definition of the nSD threshold in the Supplementary Material (Section 4), the influence of the boundary choice on the results is expected to be limited.

In the case of tortuosity, a more evident peak in the 400  $\mu\text{m}$  range can be observed in Fig. 14(d), followed by a tail towards longer lengthscale values. Since the range of tortuosity that interests pore locations is wider than the one considered in the lengthscale analysis, a difference between high tortuosity and pore distribution was expected. In particular, restricting the range of tortuosity considered corresponds to isolating parameter variations more strongly influenced by local characteristics such as meandering fibres.

The similarity assessment was based only on the locations of pores and high-tortuous regions in their evolution along the alignment direction  $z$ . This means that regions that are, for example, pore-free are not assessed in the similarity analysis. The outcome should be therefore read as an indication of the stability along  $z$  of the pore locations. The choice was made to ensure that the focus of the evaluation was only on the features analysed.

Max-filtering creates a degree of local homogenisation in the similarity analysis, which can modulate the scale of feature observation while reducing the computational time. An adequate fine-tuning of

the kernel used to extract characteristic lengthscales for specific case studies can aid in defining representative characteristics of the material. While the method development was conducted with a cubic kernel with a 15 voxel side, corresponding to about 1.5 times the fibre's diameter, different kernel size choices are expected to affect the level of homogenisation and, therefore, the similarity results. A sensitivity analysis of the kernel size and its effect on the similarity results is shown in Supplementary Material (Section 7), which highlights how the kernel size can modulate the observed scale of features, with smaller kernels capturing finer details and larger kernels highlighting broader distributions, although at the cost of increased homogenisation.

The lengthscales extracted through the similarity analysis for each microstructural feature considered could find application in the definition of Representative Volume Elements (RVE). RVE tailored to consider specific lengthscales of microstructural variability for different fibre and pore features might allow for more accurate modelling of composite prepregs. Due to the low sampling at the edges of the scan space, however, it is advisable that larger portion of the material should be assessed to the extinction of the features observed.

## 5. Conclusion

The work focused on the 3D microstructural analysis of an experimental unidirectional prepreg based on X-ray microcomputed tomography data, with a focus on the characterisation of its pore network and fibre architecture characteristics. To assess the consistency of the findings, the scan length was split into six sub-volumes in the principal fibre alignment direction to analyse the features of interest.

Pore distribution analysis indicated a tendency for both surface and internal pores to cluster in areas with increased tortuosity, indicating a complex relationship between pore evolution and fibre architecture that needs further investigation. This correlation suggests a strong connection between porosity evolution and fibre paths, and in particular potential interactions between pore distribution and meandering fibres, characterised by high tortuosity and misalignment. The results suggest that single meandering fibres can trigger larger-scale phenomena, features that might get overlooked in common homogenisation approaches typical of multiscale studies. A possible origin of meandering fibres is from the rupture of long fibres by friction during dry tow spreading, with consequent loss in tension. Early steps in the manufacturing process might, therefore, profoundly affect the final tape microstructure and lead to porosity events downstream in the process. The optimisation of the tape manufacturing process is of prime importance in controlling the final prepreg microstructure.

The quantification of characteristic lengthscales of the pore network and tortuosity along the principal alignment direction showed feature propagation across multiple sub-volumes. This work strongly indicates that the characteristic scale of feature propagation is beyond the current observation scale, emphasising the need to acquire larger volumes to assess characteristic lengthscales in unidirectional composite tapes. A deeper understanding of lengthscales of feature propagation might find application in developing more accurate representative volume elements of the tape microstructure.

The work is focused on the methodology development for the analysis of unidirectional composite tapes with complex pore structures, hence the extent to which the volume analyses is representative of the whole tape is not discussed. For a complete characterisation of a unidirectional tape and assessment of its variability, microstructural studies at multiple locations along the principal fibre direction and in the transversal direction would be advisable. Such a study could help clarify the effect of manufacturing processes that lead to the tape microstructure, and the tape performance in engineering practice.

## CRediT authorship contribution statement

**S. Gomasasca:** Writing – original draft, Validation, Methodology, Investigation, Formal analysis, Conceptualization. **D.M.J. Peeters:** Writing – review & editing, Supervision, Conceptualization. **B. Atli-Veltin:** Writing – review & editing, Supervision. **T. Slange:** Writing – review & editing, Resources. **G. Ratouit:** Writing – review & editing, Resources. **C. Dransfeld:** Writing – review & editing, Supervision, Project administration, Methodology, Conceptualization.

## Declaration of competing interest

The authors declare the following financial interests/personal relationships which may be considered as potential competing interests: Tijtse Slange and Guillaume Ratouit are employed at Toray Advanced Composites (Netherlands). This should be already visible and clear from the author affiliations, we decided to report this here for additional transparency. If there are other authors, they declare that they have no known competing financial interests or personal relationships that could have appeared to influence the work reported in this paper.

## Acknowledgements

The authors would like to acknowledge Naturalis Biodiversity Center, Leiden (NL) for conducting the data acquisition via X-ray computed tomography, and Hans Luinge for valuable support and discussion.

## Appendix A. Supplementary data

Supplementary material related to this article can be found online at <https://doi.org/10.1016/j.compositesa.2024.108669>.

## Data availability

Data will be made available on request.

## References

- [1] Schlothauer A, Pappas GA, Ermanni P. Thin-ply thermoplastic composites: From weak to robust transverse performance through microstructural and morphological tuning. *Composites B* 2023;261:110764.
- [2] Gomasasca S, Peeters D, Atli-Veltin B, Dransfeld C. Characterising microstructural organisation in unidirectional composites. *Compos Sci Technol* 2021;215(July):109030.
- [3] Çelik O, Peeters D, Dransfeld C, Teuwen J. Intimate contact development during laser assisted fiber placement: Microstructure and effect of process parameters. *Composites A* 2020;134:105888.
- [4] Slange TK, Warnet LL, Groupe WJ, Akkerman R. Deconsolidation of C/PEEK blanks: on the role of prepreg, blank manufacturing method and conditioning. *Composites A* 2018;113(July):189–99.
- [5] Amedewovo L, Orgéas L, de Parscau du Plessix B, Lefevre N, Levy A, Corre SL. Deconsolidation of carbon fiber-reinforced PEKK laminates: 3D real-time in situ observation with synchrotron X-ray microtomography. *Composites A* 2024;177:107917.
- [6] Boztepe S, Šimáček P, Labastie K, Chevalier M, Sandre P, Des J-M, Advani SG. Effect of the initial resin distribution in partially impregnated thermoplastic prepregs on consolidation. *Compos Sci Technol* 2022;225:109488.
- [7] Studer J, Dransfeld C, Jauregui Cano J, Keller A, Wink M, Masania K, Fiedler B. Effect of fabric architecture, compaction and permeability on through thickness thermoplastic melt impregnation. *Composites A* 2019;122(April):45–53.
- [8] Gomasasca S, Peeters DMJ, Atli-Veltin B, Dransfeld CA, Luinge H. The role of matrix boundary in the microstructure of unidirectional composites. In: *Proceedings of the 20th european conference on composite materials - Composites meet sustainability*. vol. 3, EPFL Lausanne, Composite Construction Laboratory; 2022, p. 636–43.
- [9] Srisuriyachot J, Bénézech J, Couégnat G, McNair SA, Maierhofer T, Butler R, Lunt AJ. Synchrotron micro-CT in kink-band formation of UD-CFRP laminates with microdefects. *Composites B* 2023;266:111038.
- [10] Mehdikhani M, Gorbatiikh L, Verpoest I, Lomov S. Voids in fiber-reinforced polymer composites: A review on their formation, characteristics, and effects on mechanical performance. *J Compos Mater* 2019;53(12):1579–669.

- [11] Mehdikhani M, Straumit I, Gorbatikh L, Lomov SV. Detailed characterization of voids in multidirectional carbon fiber/epoxy composite laminates using X-ray micro-computed tomography. *Composites A* 2019;125:105532.
- [12] Gomasca S, Peeters D, Atli-Veltin B, Dransfeld C. X-ray computed tomography of a unidirectional composite tape with microporosity features; version 1. 4tu.researchdata. 2024, <http://dx.doi.org/10.4121/b877fe30-d07f-4936-af8d-06fb78c54566.v1>.
- [13] Schindelin J, Arganda-Carreras I, Frise E, Kaynig V, Longair M, Pietzsch T, Preibisch S, Rueden C, Saalfeld S, Schmid B, Tinevez JY, White DJ, Hartenstein V, Eliceiri K, Tomancak P, Cardona A. Fiji: An open-source platform for biological-image analysis. *Nature Methods* 2012;9(7):676–82.
- [14] Arganda-Carreras I, Kaynig V, Rueden C, Eliceiri KW, Schindelin J, Cardona A, Seung HS. Trainable weka segmentation: A machine learning tool for microscopy pixel classification. *Bioinformatics* 2017;33(15):2424–6.
- [15] Tinevez JY, Perry N, Schindelin J, Hoopes GM, Reynolds GD, Laplantine E, Bednarek SY, Shorte SL, Eliceiri KW. Trackmate: An open and extensible platform for single-particle tracking. *Methods* 2017;115:80–90.
- [16] Alves M, Li Y, Pimenta S. Spatial variability and characteristic length-scales of strain fields in tow-based discontinuous composites: Characterisation and modelling. *Composites B* 2023;262(April):110789.
- [17] Sutcliffe MP, Lemanski SL, Scott AE. Measurement of fibre waviness in industrial composite components. *Compos Sci Technol* 2012;72(16):2016–23.
- [18] Hisham MB, Yaakob SN, Raof RA, Nazren AB, Embedded NMW. Template matching using sum of squared difference and normalized cross correlation. In: 2015 IEEE student conference on research and development, SCORed 2015. IEEE; 2015, p. 100–4.
- [19] Bull DR. Communicating pictures (Chapter 8 - Coding moving pictures: Motion prediction). Academic Press; 2014, p. 255–89.
- [20] Blarr J, Klinder S, Liebig W, Inal K, Kärger L, Weidenmann K. Deep convolutional generative adversarial network for generation of computed tomography images of discontinuously carbon fiber reinforced polymer microstructures. *Sci Rep* 2024;14:9641.
- [21] Arquier R, Sabatier H, Iliopoulos I, Régnier G, Miquelard-Garnier G. Role of the inter-ply microstructure in the consolidation quality of high-performance thermoplastic composites. *Polym Compos* 2024;45:1218–27.
- [22] Wood JR, Bader MG. Void control for polymer-matrix composites (1): Theoretical and experimental methods for determining the growth and collapse of gas bubbles. *Compos Manuf* 1994;5:139–47.
- [23] Vilà J, Sket F, Wilde F, Requena G, and Javier LLorca CG. An in situ investigation of microscopic infusion and void transport during vacuum-assisted infiltration by means of X-ray computed tomography. *Compos Sci Technol* 2015;119:12–9.
- [24] Latil P, Orgéas L, Geindreau C, Dumont P, du Roscoat SR. Towards the 3D in situ characterisation of deformation micro-mechanisms within a compressed bundle of fibres. *Compos Sci Technol* 2011;480–8.
- [25] Viguié J, Latil P, Orgéas L, Dumont P, du Roscoat SR, Bloch J-F, Marulier C, Guiraud O. Finding fibres and their contacts within 3D images of disordered fibrous media. *Compos Sci Technol* 2013;89:202–10.
- [26] Fast T, Scott AE, Bale HA, Cox BN. Topological and Euclidean metrics reveal spatially nonuniform structure in the entanglement of stochastic fiber bundles. *J Mater Sci* 2015;50(6):2370–98.
- [27] Hosseini S, den Otter A, Zevenbergen J, Atli-Veltin B, Dransfeld C. Methodology for the identification of hydrogen gas permeation path in damaged laminates. In: Proceedings of the 20th European conference on composite materials - Composites meet sustainability. vol. 5, EPFL Lausanne, Composite Construction Laboratory; 2022, p. 306–13.
- [28] Buser YM, Groupe WJ, Krämer E, Akkerman R. Electrical conductivity characterisation of stochastic zigzag paths in unidirectional C/PAEK. In: Proceedings of the 23th international conference on composite materials. ICCM23, vol. 27, 2023.
- [29] Irfan MS, MacHavaram VR, Mahendran RS, Shotton-Gale N, Wait CF, Paget MA, Hudson M, Fernando GF. Lateral spreading of a fiber bundle via mechanical means. *J Compos Mater* 2012;46(3):311–30.
- [30] Appel L, Kerber A, Abbas B, Jeschke S, Gries T. Determination of interactions between bar spreading process parameters and spreading quality for the development of an automated quality control of spread high modulus fiber tows. In: Proceedings of the 17th European conference on composite materials, ECCM17, 26-30th June 2016, Munich, Germany, organized by TUM, Institute for carbon composites. vol. 5 - Manufacturing Technologies, 2016.
- [31] Yi Q, Wilcox P, Hughes R. Modelling and evaluation of carbon fibre composite structures using high-frequency eddy current imaging. *Composites B* 2023;248:110343.
- [32] Auenhammer RM, Prajapati A, Kalasho K, Mikkelsen LP, Withers PJ, Asp LE, Gutkin R. Fibre orientation distribution function mapping for short fibre polymer composite components from low resolution/large volume X-ray computed tomography. *Composites B* 2024;275:111313.
- [33] Auenhammer R, Kim J, Oddy C, Mikkelsen LP, Marone F, Stampanoni M, Asp LE. X-ray scattering tensor tomography based finite element modelling of heterogeneous materials. *Npj Comput Mater* 2024;10.
- [34] Yu H, Potter K, Wisnom M. A novel manufacturing method for aligned discontinuous fibre composites (High Performance-Discontinuous Fibre method). *Composites A* 2014;65:175–85.
- [35] Laurencin T, Orgéas L, Dumont P, du Roscoat SR, Laure P, Corre SL, Silva L, Mokso R, Terrien M. 3D real-time and in situ characterisation of fibre kinematics in dilute non-Newtonian fibre suspensions during confined and lubricated compression flow. *Compos Sci Technol* 2016;134:258–66.
- [36] Sosa-Rey F, Abderrafai Y, Lewis AD, Theriault D, Piccirelli N, Lévesque M. OpenFiberSeg: Open-source segmentation of individual fibers and porosity in tomographic scans of additively manufactured short fiber reinforced composites. *Compos Sci Technol* 2022;226:109497.